ACS Catalysis

pubs.acs.org/acscatalysis
Research Article

Correlated Operando Electron Microscopy and Photoemission Spectroscopy in Partial Oxidation of Ethylene over Nickel

Claudiu Colbea, Milivoj Plodinec, Man Guo, Luca Artiglia,* Jeroen Anton van Bokhoven,* and Marc Willinger*

Cite This: ACS Catal. 2024, 14, 17850−17861
Read Online

ABSTRACT: The production of syngas from light hydrocarbons is a viable way of converting under-utilized hydrocarbon sources into valuable products until a full transition to renewable energy sources is achieved. However, current heterogeneous catalysts for syngas production suffer from deactivation, either by coking or oxidation. Here, we report on the behavior of model nickel catalysts within the context of ethylene partial oxidation and observe the catalyst-environment interaction as a function of reactant feed and temperature. Using a combination of operando microscopy and spectroscopy and focusing on a reaction regime characterized by synchronized self-sustained oscillatory dynamics, we are able to gain additional insights into the dynamic interplay between reactive species and active catalyst surfaces of varying reactivity. Real-time secondary electron imaging coupled with online mass spectrometry and thermal data shows that the oscillatory behavior is characterized by a highly active half-period during which the surface of the nickel catalyst is metallic and a less active half-period during which the surface is oxidized. Complementing the direct surface imaging, operando X-ray photoelectron spectroscopy provides missing information about the alternating chemical state of the catalyst surface in the oscillating reaction regime. It reveals that changes in the gas phase composition (C_2H_4/O_2 ratio) alter the population of reaction intermediates (e.g., carbides) on the nickel surface, which in turn drives the selectivity of the reaction toward different products. The observed chemical dynamics involve changes in gas-phase composition, rate-dependent heat of reaction, the chemical state of the catalyst, and the formation of reaction products, all of which are interconnected. Ultimately, the complex oscillations and catalytic behavior are attributed to a multistep mechanism that involves complete ethylene oxidation, dry and wet reforming of ethylene, and the reverse water gas shift reaction.

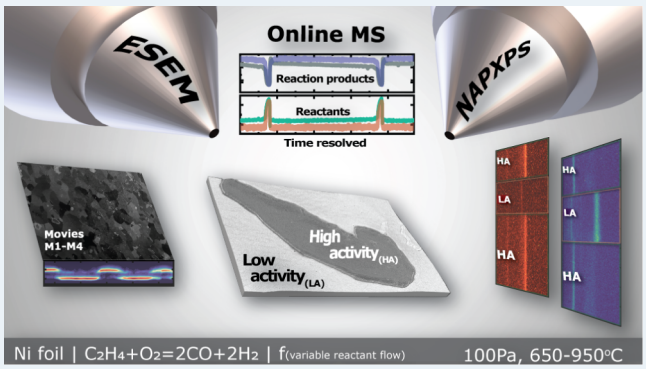

KEYWORDS: *oscillatory dynamics, ethylene partial oxidation, syngas, polycrystalline nickel foil, environmental scanning electron microscopy (ESEM), near-ambient pressure X-ray photoelectron spectroscopy (NAPXPS)*

INTRODUCTION

The production of syngas, a valuable building block for synthetic compounds,[1] relies on heterogeneous catalysts that efficiently activate both the hydrocarbon and the oxidant from the reactant source. Traditionally, noble metal catalysts such as Ru, Rh, or Ir[2,3] are employed, but due to their scarcity, more abundant non-noble metals such as Ni, Co, and Fe[4,5] have gained attention. They exhibit comparable activity but add complexity due to their susceptibility to oxidation.[6,7] Light alkanes (C1−C4) are traditionally favored for syngas production due to their abundance. In dry reforming of methane (DRM), the inherent stability of CH_4 and CO_2 requires harsh conditions, such as high temperatures and pressures, to shift the chemical equilibrium toward syngas production. While these conditions are feasible in industrial environments, they are challenging to replicate in vacuum-based characterization techniques, despite recent advancements[8] In contrast, alkenes like ethylene are more reactive due to the presence of a carbon−carbon double bond, making them more susceptible to catalytic activation under milder conditions. Additionally, the interaction of carbon-based species with the catalyst surface plays a critical role in both catalyst deactivation (through coking) and reaction dynamics. Among typical model systems, only CO oxidation provides some insights into carbon chemistry at the catalyst surface. This study focuses on the partial oxidation of ethylene to syngas over polycrystalline Ni foils as a model system. The high reactivity of Ni toward hydrocarbon activation and its well-known tendency to form carbon deposits, which can

Received: July 25, 2024
Revised: November 11, 2024
Accepted: November 12, 2024
Published: November 19, 2024

https://doi.org/10.1021/acscatal.4c04437
ACS Catal. 2024, 14, 17850−17861

deactivate the catalyst under reactive conditions, make this system particularly appealing for study. Under constant reactant feed and temperature, the system under study displays self-sustained chemical oscillations across a broad range of reaction conditions. These oscillations are defined by periodic transitions between two states with distinct product distributions, thermal effects, and catalyst structures. Chemical oscillations are abundant in catalysis[9,10] and have been explored using integral,[11−14] and localized characterization techniques,[15−17] and their kinetics have been mathematically modeled.[10,18−21] However, the mechanisms that drive the state transitions remain a subject of scientific debate. Various models, such as the oxide model,[22] the carbon model,[17,23−25] and the reconstruction model[26] have been proposed to explain the oscillatory behavior observed in elementary redox reactions. In both the oxide and carbon models, the transition between states of different activity is attributed to a gradually changing surface coverage, either by passivating oxide layers or carbon deposits, that reduces the reaction rates. Removal of these layers restores the initial activity. Conversely, the reconstruction model suggests adsorption-induced surface reconstruction, which leads to new surface structures with varying reactant coverages and activation rates. Here, we revisit the proposed mechanisms within the context of ethylene partial oxidation and observe the behavior as a function of reactant feed and temperature. By using a combination of spatially resolved real-time imaging by environmental scanning electron microscopy (ESEM), surface-sensitive near-ambient pressure X-ray photoelectron spectroscopy (NAPXPS), and online mass spectrometry (MS), we gain direct insights about the structural and chemical dynamics under operating conditions. The ESEM allows us to directly observe the surface morphology of a model catalyst in its working state under reaction conditions in real-time and at high spatial resolution. The recorded secondary electron signal does not only reveal changes in surface topology but is also sensitive to reaction-induced changes in surface composition.[27] The missing information regarding the oxidation state and chemistry of the surface is delivered by complementing synchrotron-based NAPXPS experiments that were conducted under identical gas composition, pressure, and temperature. The tunable photon energy provides chemical information regarding the catalyst surface up to a depth of a few nm and enables the identification of surface intermediates that are temporarily present during different phases of the cycling reaction at second-scale temporal resolution. The integration of real-time imaging, surface-sensitive spectroscopy, and online mass spectrometry is essential for accurately studying time-sensitive phenomena like oscillations. This approach provides new insights into the interplay between reaction- and structural dynamics that lead, through lateral coupling, to complex self-organization phenomena. In agreement with earlier studies,[17] it is found that the surface is predominantly composed of metallic Ni during periods of high activity, and NiO in the low active state. Ni_3C is detected by NAPXPS, but its role remains unclear. It is formed only under stoichiometric reactant flow at 950 °C during the transition from the low to the high activity state and continuously throughout the high activity state. Based on our findings, we propose a mechanism for the self-sustained oscillation mode in ethylene partial oxidation that involves a multistep process, including total oxidation, reverse water gas shift (RWGS), dry reforming of ethylene (DRE), and wet reforming of ethylene (WRE).

RESULTS

Polycrystalline nickel foils are first annealed in hydrogen at pressures of around 50 Pa and temperatures up to 1000 °C. High-temperature annealing induces surface reconstruction and results in a clean metallic nickel foil with a smooth surface texture (see Movie S1). Reference experiments in which metallic nickel foils are exposed to oxygen at temperatures in the range between 400 and 600 °C show that oxidation leads to a substantial increase in image brightness, caused by an increased secondary electron yield due to surface roughening and formation of small nickel oxide particles (see Figure S1).

Starting with freshly annealed Ni foils, operando SEM observations begin by setting the desired temperature and introducing the reactants with argon as a diluent at a constant flow rate of C_2H_4:O_2:Ar = 1.2:0.2:5 mL/min. Under these flow conditions, the pressure in the differentially pumped ESEM chamber equilibrates at 50 Pa. Throughout the experiment, the sample temperature is kept constant at 750 °C (pink trace in Figure 1A) by regulating the power of the laser heating stage

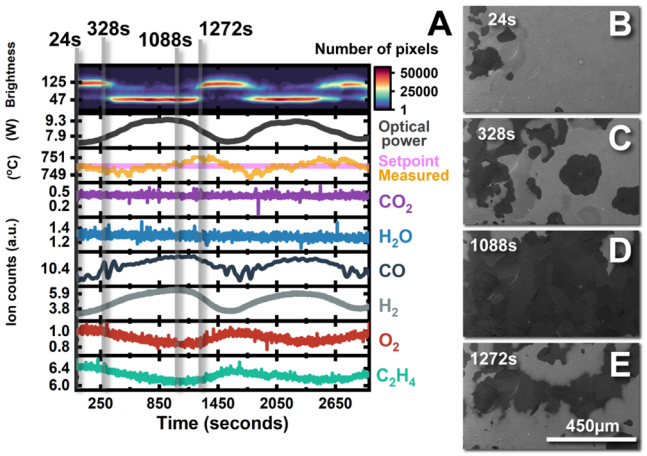

Figure 1. Self-sustained oscillations in the catalytic C_2H_4 partial oxidation to syngas over nickel foil in ESEM. (A) Integral secondary electron image brightness, heating-power, and temperature profiles plotted together with mass spectrograms of the gas composition inside the ESEM chamber under constant reactant flow of C_2H_4:O_2:Ar = 1.2:0.2:5 mL/min at 750 °C. (B−E) Selected secondary electron images collected during an oscillatory cycle at the times indicated by gray vertical lines in (A). The change in image brightness indicates the transition from oxidized (bright) to reduced nickel surface. In the reduced state (D), grain orientation contrast is visible.

(black trace in Figure 1A). In this set environment, the continuously recorded SEM images show periodic transitions between the darker, reduced nickel surface and a brighter, oxidized state (see Movie S2). Temperature fluctuations in the ESEM were controlled to within ±1 °C, as shown in Figure 1A (pink and orange traces), which corresponds to a temperature variation of only 0.1%. This minimal fluctuation has no observable impact on the brightness evolution observed in our study. Additionally, the images recorded during the high-temperature annealing process in Movie S1, were acquired at identical brightness, contrast, and detector bias settings. Despite the ∼800 °C temperature difference with respect to room temperature imaging, there was minimal variation in image quality or brightness. The diagram in Figure 1A presents the simultaneously recorded reaction-induced variation in gas-

https://doi.org/10.1021/acscatal.4c04437
ACS Catal. 2024, 14, 17850−17861

phase composition in the ESEM chamber. Also shown are the variations in image brightness, heating power, and sample temperature with reaction time. Gray vertical lines in Figure 1A indicate the moments at which the selected secondary electron (SE) images in Figure 1B−E were recorded. The presence of intrinsic oscillations is presented in Supporting Information (see Figure S2) where a detailed analysis of the oscillation behavior under different temperature control strategies is provided.

The MS data shows a periodic modulation of the reactant and product concentrations that is correlated with variations in heating power and the integral brightness of the recorded images. In the interval from t = 0 s to t = 250 s in Figure 1A, the partial pressure of the educts C_2H_4 and O_2 starts at a high level when the system is in a low activity (LA) state. With time, their concentration slowly drops due to an increasing rate of consumption. As a consequence of partial oxidation, a rise in H_2 and CO signals is observed, while the concentration of H_2O and CO_2 as products of total oxidation remains at the background level. Within this first interval, the measured temperature remains at the set value of 750 °C and is maintained via a relatively constant heating power, of around 7.3W. Throughout this low-activity state, the integral SE brightness remains high, indicating an oxidized surface. The second interval from about t = 250 s to t = 1250 s is initiated by a transition from high brightness to darker SE images. As can be seen in Figure 1C, this transition is initiated by the appearance of growing dark patches, indicating the reduction of the surface oxide layer. The change in image brightness is accompanied by a rise in C_2H_4 and O_2 consumption, as revealed by the steeper downward slope of the corresponding partial pressures in Figure 1A. At the same time, a significant rise in H_2 and CO concentrations is observed in the MS data, while the H_2O and CO_2 signals still remain close to the noise level. The transition from the bright, oxidized to a darker, reduced surface is completed after about 170s. During the whole period of high activity (HA), which lasted about 900s in the set experimental conditions, the surface remains in the metallic state, and the temperature varies around the set point by approximately ±1 °C. The deviation from the set point after the transition from the LA to the HA state is caused by the latency of the PID controller that regulates the power of the laser heating stage, and by the thermal mass of the nickel foil. Interestingly, the heating power increased during the transition from low- to high conversion from around 7.3 W to 9.2 W. The latter could be a consequence of a change in the laser absorption properties of the nickel foil upon switching from the oxidized to the metallic nickel surface. The end of the HA state and transition to the LA state is initiated by the appearance of bright patches of surface oxide in the SE images (see Figure 1D). The transition and complete surface oxidation are completed after about 80 s. Coinciding with the transition observed by ESEM, a rise in the concentration of the educt species and a drop in the product species are observed in the MS data. The succession of the HA and LA states forms a complete cycle, after which the concentrations of gaseous species, the heating power, sample temperature, and image intensity return to the same values to commence the next cycle.

In order to confirm the above assignments regarding the bright, oxidized nickel and the darker metallic surface and to detect changes in the surface chemical state and eventually identify adsorbed species, complementary synchrotron-based NAPXPS experiments are performed at the Swiss Light Source (SLS). Details on the comparison between the two experimental setups, including mass spectrometry data, temperature fluctuations, and reaction front dynamics, can be found in the Supporting Information. Experiments are conducted at different O_2 flows while maintaining a constant sample temperature of 750 °C, a constant pressure of 100 Pa and a constant flow of C_2H_4 and Ar at a ratio of 1.2:5 mL/min, respectively. The O_2 flow is stepwise increased from 0.2 to 1.2 mL/min.

Figure 2 shows variations in gas composition inside the NAPXPS chamber as detected by mass-spectrometry during

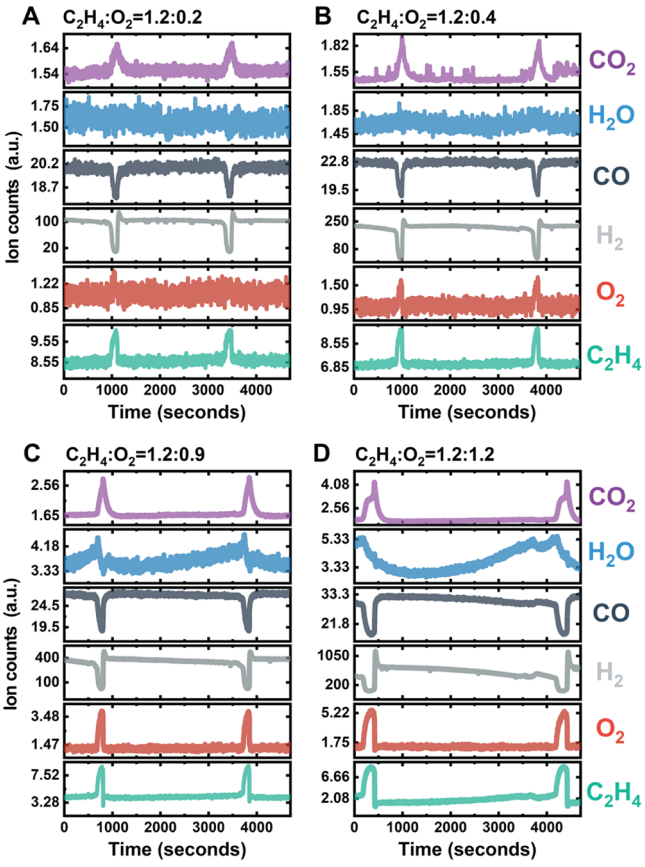

Figure 2. Mass spectrograms of the gaseous environment in the NAPXPS experimental chamber as a function of oxygen flow. The sample temperature is 750 °C while a chamber pressure of 100 Pa is maintained by supplying constant C_2H_4:Ar flows of 1.2:5 mL/min; and increasing O_2 flows: (A) 0.2; (B) 0.4; (C) 0.9; and (D) 1.2 mL/min.

ongoing reactions in the oscillating regime. In the following, unless explicitly stated, all references to reactant flow conditions will only concern oxygen, as C_2H_4 and Ar flows are kept constant throughout the experiments. Due to the smaller chamber size of the NAPXPS setup compared to the ESEM, the signals detected by MS reflect a faster response of the gas-phase concentrations to changes in catalyst activity than that in the ESEM setup.

Equation 1 is used to estimate the conversion of C_2H_4 and O_2 based on the recorded mass spectra, with I_0 as the baseline signal intensity and I_x as the signal intensity at a specific time t.[28]

https://doi.org/10.1021/acscatal.4c04437
ACS Catal. 2024, 14, 17850−17861

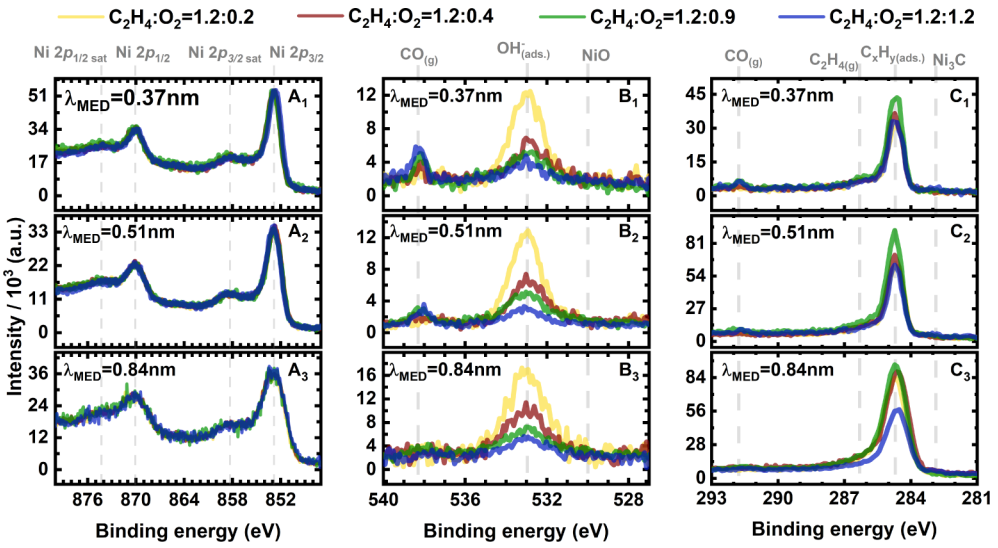

Figure 3. XPS depth profiling within the 100−500 eV kinetic energy range for Ni 2p (A_1−A_3), O 1s (B_1−B_3), and C 1s (C_1−C_3) core levels at 750 °C in the HA state. The spectra were recorded under a constant C_2H_4 flow of 1.2 mL/min while increasing the O_2 flows from 0.2 (yellow traces), 0.4 (red traces), 0.9 (green traces) to 1.2 (blue traces) mL/min.

$$\text{Conversion}\ (\%) = \frac{(I_0 - I_x) \times 100}{I_0} \quad (1)$$

Starting in an oxygen-limited regime with an oxygen flow of only 0.2 mL/min, we observe the first interval from t = 0 s to t = 920 s in Figure 2A. The system is initially in the HA state, as is indicated by a low C_2H_4 concentration (due to an estimated conversion of about 14.6%), and a near complete conversion of O_2 (as the O_2 concentration is at the noise level). Throughout the HA phase, H_2 and CO concentrations are relatively high, while the H_2O and CO_2 signals are also close to the respective noise levels. The transition from the HA to the LA state begins at t = 920 s with a sudden decrease in C_2H_4 and O_2 conversion. Over the next 136 s, the H_2 and CO signals decrease to their respective noise levels, while the H_2O signal remains relatively constant and the CO_2 signal increases. The LA state ends at t = 1056 s with a fast transition back to the HA state, in which the system stays for the next 2200 s until the next transition into the LA state happens.

When the O_2 flow is increased to 0.4 mL/min, the C_2H_4 conversion rises to 26.8% during the HA phase, while oxygen is still fully consumed (see Figure 2B). Doubling the oxygen flow leads to a substantial increase in the H_2 signal and a smaller relative increase in the CO signal. The increase in oxygen flow extends the duration of the HA state to 2700s and thus, the duration of the state during which the surface remains reduced. While the H_2O signal was hidden in the background at 0.2 mL/min of oxygen flow, a small oscillation and variation toward higher H_2O production in the LA state can be seen at an oxygen flow of 0.4 mL/min. Due to a higher oxygen flow, the CO_2 signal detected in the LA increases as well.

Upon further increase of the O_2 flow to 0.9 mL/min, the C_2H_4 conversion increases to 55.2%, and shows, during short moments in the transition from LA to the HA states, a virtually complete conversion at t = 800 and 3800 s (see Figure 2C). The O_2 conversion is no longer complete and decreases to about 98%, while the H_2 and CO production rises further. The added oxygen flow leads again to an increase in the duration of the HA state to 2900 s. Notably, the H_2O signal shows, for the first time, a synchronized variation with the activity states. Initially, in the first quarter of the HA state (t = 850−1450 s), the signal exhibits a slight negative slope and transitions to a period with constant intensity in the second quarter (t = 1450−2100s). However, in the third and fourth quarters (t = 2100−3745 s), it displays a strong positive slope; with the signal reaching its maximum shortly before the HA to LA transition. Continuing the same trend as the two previous reactant flows, the CO_2 concentration reaches higher values with increasing oxygen flow during the LA state.

Lastly, upon increasing the O_2 flow to 1.2 mL/min in Figure 2D, the C_2H_4 conversion shows short periods of virtually complete conversion during the LA to HA transition (t = 450 and 4440 s). It then stabilizes at 87% and gradually decreases to 71% toward the end of the HA state. Concurrently, the O_2 conversion decreases to 90%. Interestingly, under those reactant flow conditions, the HA and LA states show the longest duration of 3700 and 250 s, respectively. Moreover, the H_2 and CO signals reach their highest intensities among the studied gas flows. The H_2O signal now shows a double maximum, of which the first one appears toward the end of the HA phase and coincides with a slight increase in the detected H_2 and CO signal before it reaches the main peak in the transition to the LA state. The CO_2 detected in the LA phase shows now a shoulder before the peak maximum.

The observed oscillatory behavior was followed over a continuous 60-h period, during which the catalyst exhibited stable oscillations across different environmental conditions. Ex-situ experiments (data not shown) extending up to 300 h confirmed the long-term stability of this oscillatory behavior.

Figure 3 displays the X-ray photoemission spectra of Ni 2p (Figure 3A_1−A_3), O 1s (Figure 3B_1−B_3), and C 1s (Figure 3C_1−C_3) core levels that were recorded at 750 °C in the HA state, at different O_2 flow and probing depths. Spectra are plotted in different colors according to the O_2 flow rate, with yellow, red, green, and blue representing flows of 0.2, 0.4, 0.9, and 1.2 mL/min, respectively. The collected spectra with an estimated probing depth (based on specific mean escape depths (λ_{MED}) for the respective photoelectron kinetic energies) of λ_{MED} = 0.37 nm for 100 eV, λ_{MED} = 0.51 nm for 200 eV, and λ_{MED} = 0.84 nm for 500 eV are normalized to

https://doi.org/10.1021/acscatal.4c04437
ACS Catal. 2024, 14, 17850−17861

the photon flux and total cross-section. The peak broadening observed for all the core levels at larger probing depths (Figure 3A_2−C_3) is attributed to the decreased resolving power of the monochromator with the photon energy. The Ni 2p core level spectra (Figure 3A_1−A_3) show intense contributions assigned to the $2p_{3/2}$, $2p_{3/2satellite}$, $2p_{1/2}$ and $2p_{1/2satellite}$ of metallic nickel at 852.7, 858.2, 870, and 874.2 eV, respectively.[29] Their intensity is not affected by the applied changes in oxygen flow for a given probing depth. However, when comparing the signal intensity for the same O_2 flow across the probing depths, a relative decrease of 24% is observed between the spectra shown in Figure 3A_1,A_2, and an increase of 10% is observed among the spectra shown in Figure 3A_2,A_3. The nonmonotonic intensity variation is attributed to the presence of carbon- and oxygen-containing species within the sample for the MED = 0.51 nm. Together with the main core-level peaks, the Ni 2p region exhibits multiple satellite peaks, which are usually found in the 858−868 eV binding energy range. The number of such satellite peaks, due to final state effects, depends on the oxidation state of nickel.[30] The approach adopted in this work involves fitting the shakeup satellites with a single peak convolving all the possible electronic configurations and has already been used in other reports,[16,31,32] While it is not accurate from the physics point of view, it does not alter the results of the analysis because the fast transition between HA and LA (and vice versa) leads to a quantitative oxidation (reduction) of nickel.

The spectra of the O 1s core level (Figure 3B_1−B_3) show a distinctive peak at 538.1 eV, attributed to gas phase carbon monoxide CO(g)[33] and a broad peak centered at ca. 532.9 eV, marked as O(ads.). Its deconvolution, shown in Figure S3, reveals three contributions at 532.8, 531.4, and 530.3 eV, which are attributed to $OH^-_{(ads.)}$, NiO_x, and NiO respectively.[34−36] The peak at 532.8 eV in our data is assigned to OH^-(ads.), rather than adsorbed water, due to the high temperature (750 °C) and millibar pressure conditions used in our study. We recognize that OH^-(ads.) on Ni is typically reported at around 531 eV, while physisorbed water is often assigned to 532.8 eV.[30] However, under our operando conditions, it is highly unlikely that water remains in a molecularly adsorbed form. The elevated temperature and the significant pressure difference between standard XPS (UHV, room temperature) and our study would likely cause any adsorbed (physisorbed) water to desorb. Given this context, we attribute the 532.8 eV peak to OH^-(ads.) due to its strong interaction with the surface, which allows it to remain detectable at high temperatures. This assignment is consistent with previous work from our group, where we observed a similar peak under NiO reduction with hydrogen up to 1050 °C.[37] In that study, the same rationale has been applied, as physisorbed water was deemed unstable under such high-temperature conditions. Investigating operando transient evolutions on nickel foil was beyond the scope of this work. However, because relatively fast scans of the O 1s were collected at 650 °C with a C_2H_4:O_2 flow of 1.2:1.2 mL/min, we could process them with the fast Fourier transform technique (recently developed and presented in ref.[38]). This procedure helps to extract the variable part of the O 1s signal within the first seconds after the LA to HA transition and the results are shown in Figure S4. A contribution that gradually decreases is detected around 532.8 eV, which is compatible with hydroxyl groups forming and quickly recombining upon reduction of the oxide.

The intensity of the observed peaks varies monotonically with the increase in O_2 flow. The contribution from CO (g) shows an increase in intensity which is consistent with the higher CO(g) content observed in Figure 2. In contrast, the contribution of the O(ads.) shows a decrease in intensity and reveals a lower amount of oxygen-containing surface species for higher O_2 flows. Similarly, this observation is consistent with the decrease in the OH^-(ads.) to Ni $2p_{3/2}$ area ratio as shown in the brown-colored traces in Figure S5. Additionally, by increasing the probing depth, the intensity of the CO (g) contribution decreases, reaching eventually the noise level in Figure 3B_3 while the O(ads.) component increases throughout the B_1−B_2 series by 4 and 34% respectively. This increase in intensity with the increase in probing depth reveals a higher concentration of oxygen-containing species in the subsurface region.

The spectra of C 1s (Figure 3C_1−C_3) show a low-intensity feature at 292 eV that is attributed to CO(g) and a broad and complex peak centered at 286.4 eV. The deconvolution, shown in Figure S3, reveals two contributions that are attributed to $C_2H_4(g)$ at 286.4 and C_xH_y(ads.) at 284.6 eV.[39−42] Upon increasing the O_2 flow from 0.2 (yellow) to 1.2 (blue) mL/min, the CO(g) intensity increases, while C_xH_y(ads.) displays a nonmonotonic variation. Specifically, for the 0.2−0.9 O_2 flows, the intensity increases, but for the 1.2 O_2 flow it decreases to values similar to, or lower than those observed for an O_2 flow of 0.2. These observations are consistent with the increase in the area of the CO(g), C_xH_y(ads.), and $C_2H_4(g)$ components, shown in gray-colored traces in Figure S4. We refer to these species as C_xH_y(ads.) to reflect the possibility that multiple intermediates, rather than a single C_2H_4 species, are present during the reaction. The observed ±0.1 eV variation in binding energy across different O_2 flow conditions suggests that these species originate from the same parent molecule. Additionally, by increasing the probing depth, the intensity of CO(g) decreases, reaching close to noise level values in Figure C_3, while the intensity of the C(ads.) peak increases throughout the C_1−C_3 series by 111 and 115% respectively. The observed signal increase in Figure 3 C_2 is correlated with the slight signal increase in the O 1s (Figure 3B_2) and the pronounced signal decrease in the Ni 2p (Figure 3A_2) core level spectra. In line with those observations the possibility of carbon species accumulation is taken into consideration, but our results have not identified significant accumulation of specific surface species (see Figures S3, S8, and S12).[43] This topic is further addressed in the discussion section.

Figure 4 shows the O 1s (Figure 3A1−A3) and the C 1s (Figure 3B1−B3) core level peaks for a kinetic energy of 100 eV in the HA state, as a function of the O_2 flow and gas path length (GPL), which is defined as the height of the interaction cone described by the acceptance angle of the analyzer. The interaction cone represents the region where the incident photon beam interacts with the sample and the gaseous environment; and from where the generated photoelectrons are collected by the analyzer. The gas phase profiling was obtained by increasing the distance between the sample and the analyzer cone, which in turn yields a specific GPL of 0.51, 0.81, and 1.18 mm.

The gas profiling measuring mode is depicted schematically in Figure S6C, with dotted gray lines indicating the two-dimensional region from which the photoelectrons are collected. The solid−gas interface endstation allows to realign the measurement position with respect to the beamline focal

https://doi.org/10.1021/acscatal.4c04437
ACS Catal. 2024, 14, 17850−17861

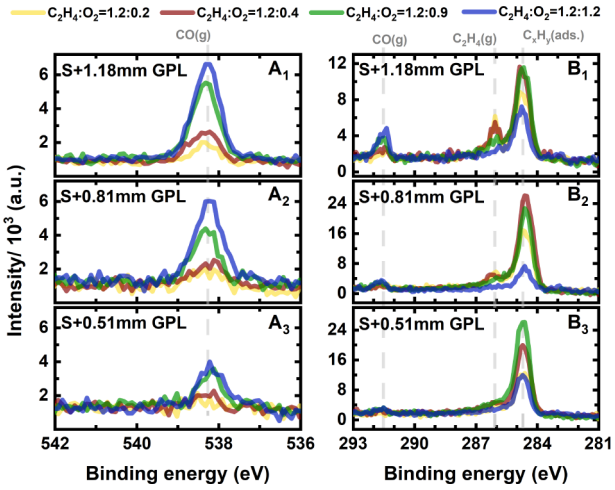

Figure 4. XPS gas phase profiling collected at 100 eV kinetic energy for O 1s (A1-A3) and C 1s (B1−B3) core levels at 750 °C. The spectra were acquired at increasing gas path lengths (GPL) by increasing the distance between the sample (S) and the analyzer differential pumping cone. The spectra were recorded under a constant C_2H_4 flow of 1.2 mL/min, while increasing the O_2 flow rates from 0.2 (yellow traces), 0.4 (red traces), 0.9 (green traces), to 1.2 (blue traces) mL/min.

spot (analyzer cone to beam distance = 0.5 mm in this case). An efficient strategy to remove the contribution of gas phase peaks to photoemission spectra is to offset the endstation by a 0.05−0.15 mm, so that the signals from the sample surface are still strong while those from the gas phase become weak. The spectra of C 1s and O 1s core levels are acquired at 100 eV kinetic energy, ensuring high photoionization cross section.[44] The displayed spectral region (542−536 eV for O 1s and 297−275 eV for C 1s) is characteristic of the photoemission signals of gas phase components. The gas phase profiling complements the depth profile spectra shown in Figure 3 and reveals a similar trend for the gaseous species. CO(g) can be observed in both O 1s and C 1s spectral regions as an intense peak at 538.1 and 292 eV respectively. Its assignment is discussed in greater detail in the Supporting Information (Figure S7). The intensity of this peak increases as the GPL increases and as the O_2 flow increases. The $C_2H_4(g)$ is observable in the C 1s spectral region at 286.4 eV. The intensity of this peak increases as the GPL increases and decreases as the O_2 flow increases. In Figure S8A, the C 1s core level profiles collected at a GPL of 1.18 mm reveal the presence of CO(g), $C_2H_4(g)$, and C_xH_y(ads.) during the HA state (0−1900s), while only $C_2H_4(g)$ is observed during the LA state (1920−2750s). Similarly, in Figure S8B, during the HA state (0−2100s), the O 1s spectral region displays signals corresponding to CO(g), H_2O(g), and OH^-(ads.). In the LA state (2150−3520s), the contribution at 530 eV, which is assigned to NiO, is clearly observable.

Figure 5 shows the X-ray photoemission spectra of Ni 2p (Figure 5A_1−A_3), O 1s (Figure 5B_1−B_3), and C 1s (Figure 5C_1−C_3) in the LA state, at 750 °C and C_2H_4:O_2 flows of 1.2:1.2, as a function of the probing depth. The spectra of Ni 2p (Figure 5A_1−A_3) show intense contributions across all probing depths in the LA state, at 855, 861.1, and 872.5 eV. They can be assigned to the $2p_{3/2}$, $2p_{3/2satellite}$, and $2p_{1/2}$ features of nickel oxide.[32] The spectra of the O 1s core level (Figure 5B_1−B_3) show an intense contribution at 530.1 eV, which is attributed to NiO.[32] The spectra of C 1s (Figure 5C_1−C3) only show noise at all probing depths. The absence of carbon-containing species in the LA state and the presence of typical, oxide-related features in the Ni and O spectral regions demonstrates the dominant presence of nickel oxide during the LA state, confirming the earlier assignment in the interpretation of the ESEM images. Furthermore, the detection of oxide peaks at all probed depths implies that the sample is oxidized within the probing depth achieved in this work of approximately 2.5 nm ($3 \times \lambda_{MED}$ = 2.52 nm). Consistent with previous research, the oxide film thickness during an oscillation cycle can extend up to 10 μm, while the core of the foil retains its metallic state.[45,46] Movie S4 complements the thickness estimation and follows several reduction waves during the transition from LA to HA states. The absence of visible gas-phase peaks for C_2H_4 and O_2 in Figure 5B1−C3 is attributed to the different measurement strategies employed during our NAPXPS experiments. We used two strategies: one aimed at maximizing the sample signal by reducing the sample-analyzer cone distance, and another aimed at maximizing the gas-phase

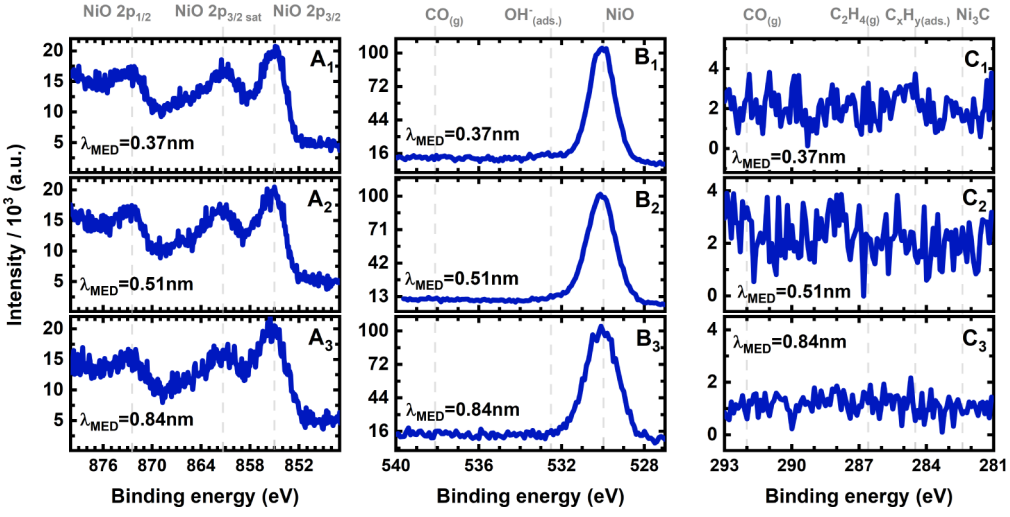

Figure 5. XPS depth profiling within the 100−500 eV kinetic energy range for Ni 2p (A_1−A_3), O 1s (B_1−B_3), and C 1s (C_1−C_3) core levels at 750 °C and a C_2H_4:O_2 flow of 1.2:1.2 mL/min in the LA state.

https://doi.org/10.1021/acscatal.4c04437
ACS Catal. 2024, 14, 17850−17861

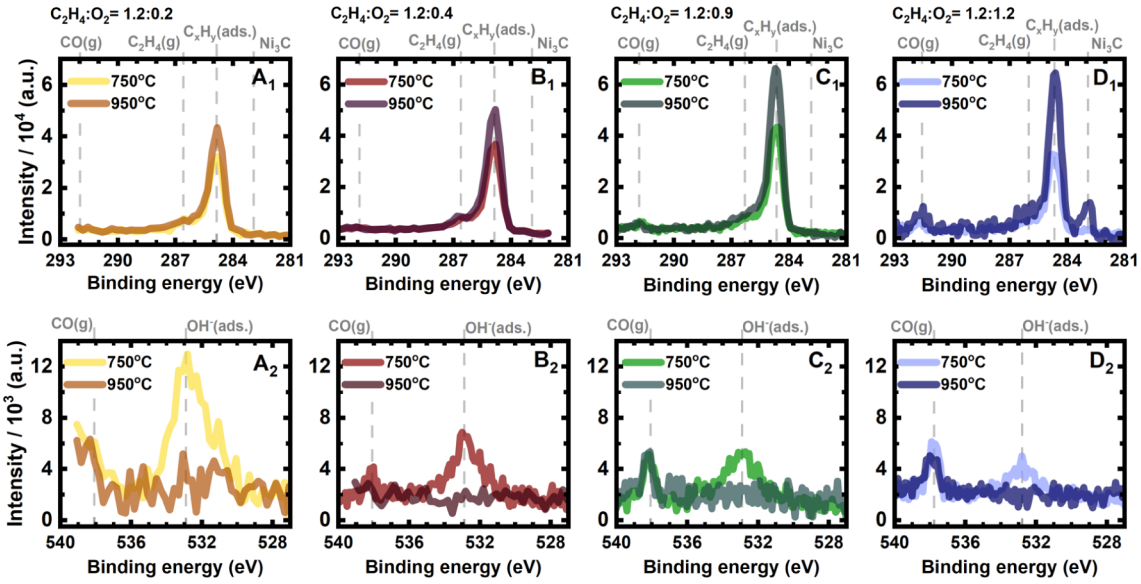

Figure 6. X-ray photoelectron spectra of the C 1s (A_1−D_1) and O 1s (A_2−D_2) core levels as a function of the C_2H_4:O_2 flows and catalyst temperature (750 and 950 °C). The color coding of the C_2H_4:O_2 flows corresponds with the one used in Figures 2 and 3 (C_2H_4:O_2 = 1.2:*x*; where *x* = 0.2, 0.4, 0.9, and 1.2 corresponds to yellow, red, green, and blue, respectively). The spectra collected at 950 °C are represented in darker shades.

signal by varying this distance. In the latter approach, increasing the gas path length (GPL) enhances the gas-phase signals while weakening the sample signals. Using this strategy, the gas-phase signals for reactants and products can be observed. The effectiveness of this approach is illustrated in Figure 4B1−B3, where the intensities of CO(g) and C_2H_4 (g) increase as the intensity of C_xH_y(ads.) decreases with increasing GPL, aiding in distinguishing between gas-phase components and sample components in the complex photoemission spectra. Similarly, Figure S8B shows weak signals for O_2 (g) and C_2H_4(g) during the LA state, even with a strategy designed to maximize gas-phase signals.

Figure 6 shows the C 1s (Figure 5A_1−D_1) and O 1s (Figure 5A_2−D_2) core level spectra in the HA state, collected at a fixed kinetic energy of 100 eV, as a function of the set C_2H_4:O_2 flows and temperature. The same intensity scale is displayed for all the spectra to facilitate the comparison between the eight sets of experimental conditions. At 950 °C, the C 1s spectral region shows an increase in the signal intensity that amounts to 24, 29, 40, and 83% compared to the spectra collected at 750 °C at the respective gas ratios. Moreover, Figure 6D_1 shows the appearance of a peak at ∼283 eV that is attributed to Ni_3C.[46] The O 1s show an opposite behavior upon increasing the catalyst temperature. The intensity of CO(g) remains relatively constant across the first three gas ratios and decreases by ∼15% for 1.2 O_2 flow. The signal intensity of O(ads.) peaks centered at ∼532.9 eV decreases to noise levels across all the O_2 flows when the catalyst temperature is increased to 950 °C. As the O_2 flow or temperature increases, the overall reaction rate rises, leading to higher production of H_2 and CO (see Figures 2 and S9). This increased production results in a greater coverage of C_xH_y(ads.) species on the catalyst surface, which is evident from the increased intensity of the C 1s peak with higher O_2 concentration or temperature (see Figure 6). The observed trend, where the O(ads.) peak intensity decreases while the C_xH_y(ads.) peak intensity increases, indicates an inverse correlation between O(ads.) and catalytic activity. In higher catalytic activity states, the sites that would typically be occupied by O(ads.) are instead taken up by C_xH_y(ads.) species. This assumption is supported by the fact that the interaction between carbon-containing species and the nickel surface is stronger than that between O(ads.) and the surface.[47]

DISCUSSION

We observed a dynamically changing structure of a nickel catalyst during self-sustained oscillations in C_2H_4 partial oxidation to syngas under different reaction conditions. The periodic switching of the catalytic surface between HA and LA states alters the composition of the gas phase and boundary layer above the catalyst surface and vice versa. Through direct SE imaging combined with online mass spectrometry and supporting complementary operando photoemission spectroscopy, we confirm that the HA state corresponds to a metallic Ni surface and the LA state to a NiO-covered surface.

Based on the observed periodical changes in gas-phase composition and surface chemical composition in the HA and LA states, measured as a function of probing depth, mixing ratio, and temperature, we propose the following multistep reaction mechanism. The initial phase of the HA state involves total ethylene oxidation (eq 2), while the subsequent step branches into dry and wet reforming of the remaining ethylene (DRE, eqs 3 and 4 and WRE, eqs 5 and 6, respectively) and reverse water gas shift (RWGS, eq 7) between the formed products.

$$C_2H_4 + 3O_2 \rightleftharpoons CO_2 + H_2O \quad (2)$$

$$C_2H_4 + 2CO_2 \rightleftharpoons 4CO + 2H_2 \quad (3)$$

$$C_2H_4 + 4CO_2 \rightleftharpoons 6CO + 2H_2O \quad (4)$$

$$C_2H_4 + 2H_2O \rightleftharpoons 2CO + 4H_2 \quad (5)$$

$$C_2H_4 + 4H_2O \rightleftharpoons 2CO_2 + 6H_2 \quad (6)$$

$$CO_2 + H_2 \rightleftharpoons CO + H_2O \quad (7)$$

https://doi.org/10.1021/acscatal.4c04437
ACS Catal. 2024, 14, 17850−17861

The mass spectrograms show that as the O_2 flow increases, the C_2H_4 conversion also increases (Figure 1A−D), which yields H_2O and CO_2 in the initial step (eq 2). Assuming the WRE rate (eqs 5 and 6) remains relatively constant (see Figure S11), the rate of the RWGS branch (eq 7) increases, leading to a net increase of H_2O in the gaseous environment. This is observed as the positive slope of the H_2O MS signal (Figure 2C, t = 1000−3500 s; Figure 2D, t = 550−4000 s). In the LA state, the rate of the first step (eq 2) is low and all the subsequent reactions slow down. The result of the decreased reaction rates is observed as an increase in the reactant concentrations (Figure 2A, t = 920−1100 s). The resulting incomplete conversion favors the production of total oxidation products of ethylene, as evidenced in Figure 2D, t = 100−500 s. However, during the LA state, ethylene conversion is significantly lower. Additionally, reactions such as DRE, WRE, and RWGS do not occur in the absence of the metal. Therefore, the products detected in the MS result from eq 2, which operates at a reduced rate on NiO. At a constant O_2 flow, increasing the temperature from 750 to 950 °C increases the rate of RWGS (eq 7), as observed in the H_2O signal shown in Figure S9A_1−C_2 and the thermodynamic data shown in Figure S11C−F. The phase portraits depicted in Figure S10 illustrate the dependence between O_2 and H_2 MS signals relative to C_2H_4 and show hysteresis loops that reflect the stability of the system in the HA and LA states. At elevated temperatures, under identical gas conditions, the branches of the hysteresis loop are sharply defined and indicate either a smooth transition between the two states (as seen in Figure S10A_1,A_2) or a bimodal distribution (as seen in Figure S10C_1,C_2).

In the proposed reaction mechanism, the reaction rates change between the HA and LA states as a consequence of the changes in the catalyst chemical state. During the HA state, the dominant surface species is metallic Ni, whereas in the LA state, NiO is present. Furthermore, during the LA state, no carbon-containing species are detected on the surface and subsurface (Figure 5C_1−C_3). Given that the XPS probing depth is approximately three times the mean escape depth of photoelectrons, the changes in the catalyst structure exceed a layer thickness of 2.5 nm. XPS depth profiling and SEM images imply that the state switch between the HA and LA involves the surface and the bulk of the catalyst. Interestingly, upon increasing the O_2 flow (as shown in Figure 3C_1−C_3) or temperature (as shown in Figure 6A_1−D_1), the contribution of oxygen-containing species decreases, while the contribution of carbon-containing species increases. Water in the gas phase is generated as a byproduct of the partial oxidation of ethylene to syngas under the given experimental conditions. Since hydroxyl recombination and water desorption is promoted under these conditions, no increase of hydroxyl species on the catalyst surface is observed.[48,49] Production of H_2 and CO. This in turn increases the surface coverage of C_xH_y(ads.) species, as reflected by the increased intensity of the C 1s peak at higher O_2 concentrations or temperatures. This suggests that ethylene activation is likely the rate-determining step, with ethylene intermediates having a long enough lifetime to be detected by XPS. In contrast, the coverage of hydroxyl groups remains low, and their recombination likely occurs instantaneously. Furthermore, the observed trend, where the O(ads.) peak intensity decreases while the C_xH_y(ads.) peak intensity increases, points to an inverse correlation between O(ads.) and catalytic activity. In states of higher catalytic activity, surface sites that would typically be occupied by O(ads.) are instead taken up by C_xH_y(ads.) species, reflecting the shift in surface chemistry during the more active phases of the reaction."

Under the highest O_2 flow of 1.2 mL/min and 950 °C, Ni_3C is observed on the surface during the end of the LA state and the beginning of the HA state, as shown in Figures 6D1, 7, and S12.

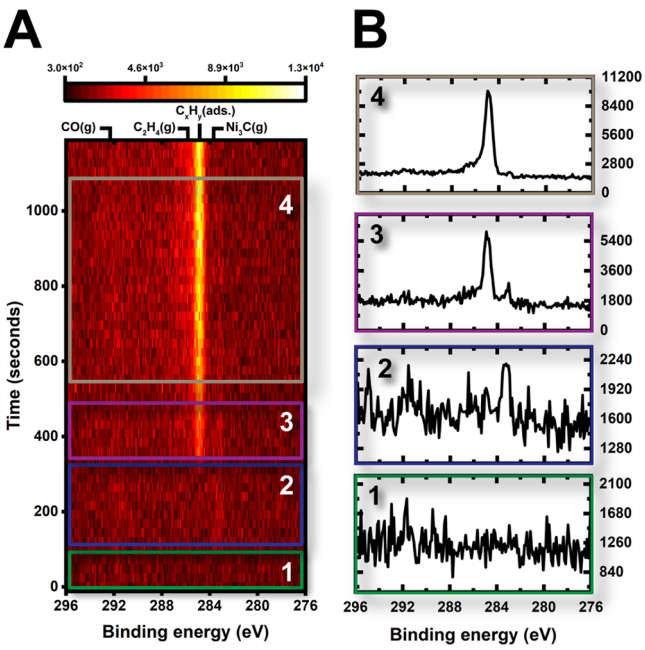

Figure 7. Presence of Ni_3C on the surface during LA−HA transition under an C_2H_4:O_2 flow of 1.2:1.2 and 950 °C. (A) Time-resolved spectra of the C 1s core level. (B) Averaged and normalized C 1s spectra extracted from the temporal region visually indicated by color and number-coded rectangles.

The temporal evolution of the Ni_3C peak, illustrated in Figure 7, follows four stages: absence, appearance, fading, and disappearance. The presence of carbide species was unexpected, given the general instability of carbides under high temperatures and oxygen-containing environments.[50−52] Previous studies indicate that the carbon source in Ni_3C synthesis influences its growth characteristics. Specifically, when using C_2H_4[52,53] as a reactant, carbide formation occurs preferentially at terrace sites, without quantifiable bulk diffusion. In contrast, the use of CO[54−56] as reactant results in the formation and subsequent diffusion of carbide into the subsurface.

During a complete oscillation cycle, C_2H_4 and O_2 concentrations are highest within the last 250 s of the LA state, as reactants are not consumed. In this state, the NiO surface is stochastically reduced, locally forming fresh metallic sites that catalyze an exothermic reaction, observed as a spike in Figure S9C_2 in the average sample temperature. It is reasonable to assume that the local gaseous composition above those sites is depleted in reactants and enriched in products, when compared to the overall gaseous composition in the experimental chamber. Also, during the transition, the overall chamber composition shows the highest concentration of H_2 and CO and the lowest concentration of C_2H_4 and O_2. Collectively, the temperature spike and the local gaseous composition promote the formation of Ni_3C. After the initial

https://doi.org/10.1021/acscatal.4c04437
ACS Catal. 2024, 14, 17850−17861

stages of the HA state, the system enters a quasi-stable regime, with incomplete O_2 conversion and stable temperature of 950 °C. During this state, the Ni_3C gradually fades, completely disappearing completely disappearing withing the following 500 s.

In this context, the detection of Ni_3C is attributed to a short, positive imbalance between its rates of formation and decomposition during the transition between the LA and HA states. Hence, considering that Ni_3C is observed exclusively at high temperatures and under the highest oxygen flow, i.e., conditions associated with the highest conversion, we assign the source of Ni_3C to the catalytic dissociation of CO that is generated during the ethylene to syngas reaction. Its absence under low O_2 flow conditions at 950 °C is attributed to insufficient CO concentration, coupled with high decomposition rates. At the highest O_2 flow of 1.2 mL/min, although the decomposition rate is at its peak, the CO concentration is also highest. This allows Ni_3C to form in sufficient amount to be detected, as momentarily its formation rate surpasses its decomposition rate. Moreover, the absence of Ni_3C from subsurface regions under all O_2 flow conditions indicates that the decomposition rate is indeed very high, effectively decomposing the surface carbide before it can be incorporated into the bulk.

Several models have been proposed to explain periodic oscillations in heterogeneous catalytic systems. Among these, three are predominantly employed to explain the oscillatory behavior in alkane oxidation catalyzed by transition metals: the reconstruction model, the oxide model, and the carbon model. The reconstruction model suggests that under different environmental conditions, only the arrangement of atoms in the topmost surface layers is modified, while the bulk crystallographic orientation of the grain remains the same. This, in turn, influences the sticking coefficients of the gaseous species and therefore alters the composition of the adsorbed layer that will participate in the catalytic reaction. The oxide and carbon models share similarities, as they both attribute the state switching to the accumulation of passivating oxide layers or carbon deposits. However, none of these models can be directly applied to explain the observed state switching presented in this work. The reconstruction model suggests only surface reconstruction, whereas our findings indicate that the state transitions involve a layer that extends at least 2.5 nm in thickness, thus approaching the bulk. As for the oxide model, it anticipates the existence of an oxide layer during the LA state. Under higher O_2 flows, it predicts a faster accumulation of the passivating oxide species that would lead to a shorter HA state. Indeed, during the LA state, we observe NiO as the dominant surface species. However, our experimental data (Figure 2) show that the duration of the HA state increases from 2200 to 2700, 2900, and 3700 s as the O_2 flow increases from 0.2 to 0.4, 0.9, and 1.2 mL/min. Furthermore, the state transitions are also observed at 950 °C, a temperature at which no oxygen-containing surface species are present (Figure 6 A_2−D_2). Regarding the carbon model, it predicts surface deactivation by carbon species during the LA state and a slower accumulation of passivating carbon-containing species at higher O_2 flows. Our results show that the duration of the HA state increases for higher O_2 flows, as correctly predicted by the carbon model, but during the LA state, there are no carbon-containing species detected on the surface (Figure 4C_1−C_3).

Therefore, we describe the HA−LA state transition through a hybrid mechanism that is schematically depicted in Figure 8

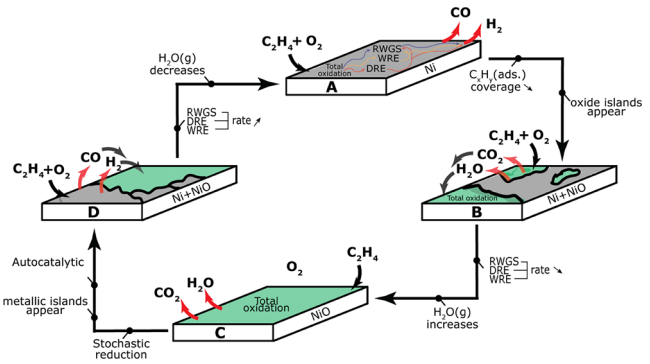

Figure 8. Schematic representation of the interaction between the gas phase and the structural dynamics of the nickel surface during the transition from HA (A) to LA (C) states in the partial oxidation of ethylene over polycrystalline Ni. The proposed mechanism includes total oxidation in the first step and dry reforming of ethylene (DRE), wet reforming of ethylene (WRE) and reverse water gas shift (RWGS) in the second step.

and combines aspects of the oxide and carbon models. During the HA state, the presence of carbon-containing species that are attributed to intermediates originating from reacted ethylene shows that ethylene is activated on the metallic Ni surface. These intermediates react with activated oxygen species and form, in the initial stage, thermodynamically favored total oxidation products (Figure 8A). Subsequently, in the second stage, the products formed in the first stage further react on metallic Ni with surface ethylene intermediates through a combination of RWGS, DRE, and WRE pathways. Throughout the HA state, the signal intensity of carbon-containing surface species decreases, as shown in Figure S12A−C (see the line profiles). Given the constant presence of O_2 in the gas phase and the variable production of water from the catalytic reaction, the observed decrease in carbon-containing species is not unexpected. The observed rate of decrease of the carbon-containing species varies as a function of probing depth and it is likely that carbon-containing species are present at higher concentrations in the subsurface regions since their etching by the oxidizing agents in the gas phase. is less effective than on the surface. Simultaneously, an imbalance in the reaction rates causes a gradual increase in the water concentration in the gas phase (Figure S8B) via the RWGS reaction. Water in the gas phase reacts with the intermediates originating from reacted ethylene, exposing fresh metallic sites that rapidly oxidize to form nickel oxide islands (Figure 8B). These sites further increase the imbalance in the reaction rate causing water to accumulate in the gas phase until the transition to the LA state is triggered. Water is thus triggering the switch from the active metallic to the inactive oxidized surface state. During the transition, synchronization across multiple sites is done through the gas phase which is now rich in water and reactants. As schematically illustrated in Figure 8C, the catalyst in the LA state retains slight activity, with CO_2 and H_2O signals being unambiguously detected in the mass spectrograms (Figure 2). During the LA state, the partial pressure of ethylene increases, and the rate at which ethylene molecules stochastically reduce nickel oxide to metallic nickel increases toward the end of the LA state, leading to the

https://doi.org/10.1021/acscatal.4c04437
ACS Catal. 2024, 14, 17850−17861

generation of fresh reactive metallic sites. With the higher reaction rate of DRE, WRE, and RWGS on metallic sites and the low concentration of water in the gas phase, the reaction reignites and starts the transition to the HA state through an autocatalytic surface process that generates more metallic sites (Figure 8D). The rates of RWGS, DRE, and WRE continue to increase as the surface coverage of nickel oxide decreases, and the cycle is closed.

CONCLUSIONS

Environmental SEM, NAPXPS, and MS confirm a, previously described, dynamically changing structure of the catalyst during self-sustained oscillations in the C_2H_4 partial oxidation to syngas. Under the experimental conditions employed in this study, we confirm, that metallic Ni is the dominant phase present during the HA state. During the LA state, the catalyst's surface is covered by an oxide layer. We have established that carbon species are directly connected to catalytic activity, while the presence of nickel oxide is inversely correlated with catalytic activity.

Our findings reveal that oscillatory states in ethylene partial oxidation are driven by a sequence of reactions. In the first stage, only complete ethylene oxidation occurs. In the second stage, the unreacted reactants and first-stage products further react and branch into RWGS, DRE, and WRE reactions. Particularly under oxygen-deficient conditions, these reactions proceed at different rates. This leads to the accumulation of hydrocarbon intermediates C_xH_y(ads.) on the catalyst surface and water in the gas phase. The transition from the HA to LA states occurs after the C_xH_y(ads.) reservoir is depleted and water accumulation reaches a critical threshold. The reaction reignites, as the catalyst surface shifts from the LA to the HA state once the water in the gas phase depletes and the concentration of reactants increases during the inactive half-period.

Overall, these findings demonstrate the intricate interplay between surface chemical states, reaction dynamics, and reaction-induced changes in gas-phase composition and provide insights into complex self-organizing systems.

MATERIALS AND METHODS

The sample consisted of a 3 × 3 × 0.5 mm Ni foil (Puratronic, 99.9945%). A K-type thermocouple was spot-welded to the back of the sample, and the temperature reading was calibrated with 0.1% accuracy. Before the experiments, the sample was cleaned in the analysis chamber in a hydrogen gaseous atmosphere at 50 Pa and up to 1000 °C. The cleaning procedure was followed by an examination of the surface's evolution in an Ar environment. This strategy was used to confirm the surfacès stability in the absence of H_2 and to guarantee that no artifacts were created because of the transition between the two reactive atmospheres, as well as to offer maximal sensitivity for the reaction products in the mass spectrum. H_2, H_2O, C_2H_4, CO, O_2, Ar, CO_2, and their associated m/z ratios of 2, 18, 27, 28, 32, 40, and 44 are the MS signals that were tracked throughout the experiment. The displayed CO signal in Figure 1 was filtered using a FFT cutoff frequency filter of 0.023. To address the issue of overlapping mass spectrum fragments for CO_2, CO and C_2H_4, we utilized fragmentation patterns obtained from NIST database and considered the intensity ratios between the primary and secondary fragments in our analysis.[57−59] For CO_2, the intensity ratio between the m/z = 44 and m/z = 28 is 9999:981; while for C_2H_4, the ratio between the m/z = 28 and m/z = 27 is 9999:6236.

We applied eq 8 to the raw data to isolate the CO contribution from the complex m/z = 28 signal

$$\mathrm{CO} = m/z\ 28(\mathrm{total}) - (\mathrm{CO_2}\ (m/z\ 44) \times 0.098) - (\mathrm{C_2H_4}\ (m/z\ 27) \times 1.6) \quad (8)$$

In-situ ESEM experiments were conducted at the ETH Zurich's Scientific Center for Optical and Electron Microscopy in a modified Thermo Fisher Scientific Quattro S SEM. A custom-developed heating stage was employed for the experiments. The microscopes vacuum generating system was upgraded to attain a base pressure of 1×10^{-5} Pa. An analytical nozzle situated 10 mm above the sample and coupled to a quadrupole mass spectrometer (Pfeiffer Vacuum PrismaPro) monitored the gaseous environment in the SEM chamber. ImageJ software package was used to process the image series into movies and to synchronize the temperature and mass spectrometric data with the corresponding image frames. Movie S1 plays at 30 frames per second, with each frame captured over 8 s.

NAPXPS measurements were carried out at the In-situ Spectroscopy beamline (X07DB) at the Swiss Light Source using the solid−gas interface chamber (SGIC) connected to a Scienta R4000 HiPP-2 ambient pressure electron energy analyzer.[60,61] Photoemission spectra were collected using linearly polarized light and a pass energy of 50 eV. The gaseous atmosphere was monitored using a quadrupole mass spectrometer (QMS) located in the second differential pumping stage of the analyzer. IgorPRO software was used to process the spectra. The spectra were normalized by the number of scans to reflect the average signal strength. A Shirley background was subtracted for quantification reasons, and the total peak areas were obtained via numerical integration. The binding energy scale of all spectra was aligned to the cleaned sample's Ni valence band (Fermi edge). All XPS data intensities were cross-section compensated, incorporating the linear polarization and asymmetry correction parameters, and their area was normalized to the photon flux. The TPP2M software tool was used to calculate the inelastic mean free path.

To ensure comparable reaction conditions between the two experimental setups, a constant gas hourly space velocity (GHSV) was maintained by using the same gas feeding system, which allows for continuous reactant mixing and precise flow regulation. In the NAPXPS setup, the gas flow was set to the minimum measurable value on the flow meter, whereas in the ESEM setup, it was adjusted to the maximum allowable value. The maximum gas flow deliverable to the experimental chambers is inherently limited by the gas feeding system and resulted in a chamber pressure of 50 Pa for the ESEM setup and 100 Pa for the NAPXPS setup. Additionally, the achievable gas flow is influenced by the pumping speeds in the differentially pumped chambers of the ESEM and NAPXPS systems. While adjustments to the experimental parameters (e.g., reducing the aperture size in the differential pumping systems or lowering the turbomolecular pump speed) could be used to regulate the maximum achievable gas flow, these modifications are impractical given the constraints of the experimental setups.

Direct heating of the sample inside the ESEM and NAPXPS chambers,[37] which resembles a cold-wall reactor setup,

https://doi.org/10.1021/acscatal.4c04437
ACS Catal. 2024, 14, 17850−17861

simplifies the study of the oscillating reaction and allows the separation of the sample's pure catalytic action from thermally activated secondary gas-phase reactions.

■ ASSOCIATED CONTENT

Supporting Information

The Supporting Information is available free of charge at https://pubs.acs.org/doi/10.1021/acscatal.4c04437.

Detailed analyses of catalyst oscillations under different PID control modes, a comparison between the ESEM and NAPXPS setups, and additional figures on NAPXPS data (photoemission spectral evolution, peak assignments, frequency-selective data analysis, and gas-phase composition) (PDF)

Movie S1: Sample preparation: high-temperature annealing in H_2 up to 900 °C (MP4)

Movie S2: ESEM movie of oscillatory dynamics at 750 °C, under a constant flow of C_2H_4:O_2:Ar = 1.2:0.2:5 mL/min (MP4)

Movie S3: ESEM movie of surface state evolution under the PID control modes described in Figure S2 (MP4)

Movie S4: ESEM movie of surface dynamics and high magnification follow-up of reduction waves during the transition from LA to HA states (MP4)

■ AUTHOR INFORMATION

Corresponding Authors

Luca Artiglia − *Laboratory for Catalysis and Sustainable Chemistry, Paul Scherrer Institute, Villigen 5232, Switzerland;* orcid.org/0000-0003-4683-6447; Email: luca.artiglia@psi.ch

Jeroen Anton van Bokhoven − *Laboratory for Catalysis and Sustainable Chemistry, Paul Scherrer Institute, Villigen 5232, Switzerland; Institute for Chemical and Bioengineering, Department of Chemistry and Applied Biosciences, ETH Zurich, Zürich 8093, Switzerland;* orcid.org/0000-0002-4166-2284; Email: jeroen.vanbokhoven@chem.ethz.ch

Marc Willinger − *Scientific Center for Optical and Electron Microscopy, ScopeM, ETH Zürich, Zürich 8093, Switzerland; Electron Microscopy with research emphasis on Energy Materials, Department of Chemistry, Technical University of Munich, Garching bei München 85748, Germany;* orcid.org/0009-0007-9913-3020; Email: marc.willinger@tum.de

Authors

Claudiu Colbea − *Scientific Center for Optical and Electron Microscopy, ScopeM, ETH Zürich, Zürich 8093, Switzerland; Institute for Chemical and Bioengineering, Department of Chemistry and Applied Biosciences, ETH Zurich, Zürich 8093, Switzerland*

Milivoj Plodinec − *Scientific Center for Optical and Electron Microscopy, ScopeM, ETH Zürich, Zürich 8093, Switzerland; Institute for Chemical and Bioengineering, Department of Chemistry and Applied Biosciences, ETH Zurich, Zürich 8093, Switzerland*

Man Guo − *Laboratory for Catalysis and Sustainable Chemistry, Paul Scherrer Institute, Villigen 5232, Switzerland; Institute for Chemical and Bioengineering, Department of Chemistry and Applied Biosciences, ETH Zurich, Zürich 8093, Switzerland*

Complete contact information is available at: https://pubs.acs.org/10.1021/acscatal.4c04437

Notes

The authors declare no competing financial interest.

■ REFERENCES

(1) Zhao, S.; et al. Recent advances on syngas conversion targeting light olefins. *Fuel* **2022**, *321*, 124124.

(2) Wei, J.; Iglesia, E. Structural requirements and reaction pathways in methane activation and chemical conversion catalyzed by rhodium. *J. Catal.* **2004**, *225* (1), 116−127.

(3) Rostrupnielsen, J. R.; Hansen, J. H. B. CO2-reforming of methane over transition metals. *J. Catal.* **1993**, *144* (1), 38−49.

(4) Joo, S.; Seong, A.; Kwon, O.; Kim, K.; Lee, J. H.; Gorte, R. J.; Vohs, J. M.; Han, J. W.; Kim, G. Highly active dry methane reforming catalysts with boosted in situ grown Ni-Fe nanoparticles on perovskite via atomic layer deposition. *Sci. Adv.* **2020**, *6* (35), No. eabb1573.

(5) Palmer, C.; et al. Dry reforming of methane catalysed by molten metal alloys. *Nat. Catal.* **2020**, *3* (1), 83−89.

(6) Wittich, K.; et al. Catalytic dry reforming of methane: Insights from model systems. *ChemCatchem* **2020**, *12* (8), 2130−2147.

(7) Sandoval-Diaz, L. E.; Schlögl, R.; Lunkenbein, T. Quo vadis dry reforming of Methane?—A review on its chemical, environmental, and industrial prospects. *Catalysts* **2022**, *12* (5), 465.

(8) Stoltze, P.; Nørskov, J. K. Bridging theundefined pressure gap" between ultrahigh-vacuum surface physics and high-pressure catalysis. *Phys. Rev. Lett.* **1985**, *55* (22), 2502.

(9) Schüth, F.; Henry, B. E.; Schmidt, L. D. Oscillatory reactions in heterogeneous catalysis. *Adv. Catal.* **1993**, *39*, 51−127.

(10) Imbihl, R.; Ertl, G. Oscillatory kinetics in heterogeneous catalysis. *Chem. Rev.* **1995**, *95* (3), 697−733.

(11) Bychkov, V. Y.; et al. Autonomous and forced oscillations during methane oxidation over cobalt catalysts. *Appl. Catal., A* **2007**, *321* (2), 180−189.

(12) Bychkov, V. Y.; et al. New oscillating system: CO oxidation over Ni. *Catal. Lett.* **2018**, *148*, 653−659.

(13) Slinko, M. M. Oscillating reactions in heterogeneous catalysis: What new information can be obtained about reaction mechanisms? *Catal. Today* **2010**, *154* (1−2), 38−45.

(14) Bychkov, V. Y.; et al. Self-Oscillations During Ethylene Oxidation Over a Ni foil. *Catal. Lett.* **2018**, *148*, 3646−3654.

(15) Suchorski, Y.; et al. Resolving multifrequential oscillations and nanoscale interfacet communication in single-particle catalysis. *Science* **2021**, *372* (6548), 1314−1318.

(16) Sandoval-Diaz, L.; et al. Metastable nickel−oxygen species modulate rate oscillations during dry reforming of methane. *Nat. Catal.* **2024**, *7* (2), 161−171.

(17) Suchorski, Y.; et al. Surface-structure libraries: Multifrequential oscillations in catalytic hydrogen oxidation on rhodium. *J. Phys. Chem. C* **2019**, *123* (7), 4217−4227.

(18) Zeininger, J.; et al. Reaction modes on a single catalytic particle: Nanoscale imaging and micro-kinetic modeling. *ACS Catal.* **2022**, *12* (20), 12774−12785.

(19) Franck, U. F. Chemical oscillations. *Angew. Chem., Int. Ed. Engl.* **1978**, *17* (1), 1−15.

(20) Slinko, M. M.; et al. Mathematical modeling of complex oscillatory phenomena during CO oxidation over Pd zeolite catalysts. *J. Chem. Phys.* **1999**, *111* (17), 8105−8114.

(21) Makeev, A. G.; et al. Mathematical modeling of oscillations during CO oxidation on Ni under reducing conditions. *Chem. Eng. Sci.* **2019**, *207*, 644−652.

(22) Turner, J. E.; et al. Oscillatory oxidation of CO over Pd and Ir catalysts. *Surf. Sci.* **1981**, *109* (3), 591−604.

(23) Burrows, V. A.; et al. Studies on self-sustained reaction-rate oscillations I: Real-time surface infrared measurements during oscillatory oxidation of carbon monoxide on platinum. *Surf. Sci.* **1985**, *160* (1), 122−138.

(24) Burrows, V. A.; et al. Studies on self-sustained reaction-rate oscillations II: The role of carbon and oxides in the oscillatory oxidation of carbon monoxide on platinum. *Surf. Sci.* **1987**, *180* (1), 110−135.
(25) Collins, N. A.; et al. Studies on self-sustained reaction-rate oscillations III: The carbon model. *Surf. Sci.* **1987**, *180* (1), 136−152.
(26) Ertl, G.; et al. Kinetic oscillations in the platinum-catalyzed oxidation of CO. *Phys. Rev. Lett.* **1982**, *49* (2), 177−180.
(27) Seiler, H. Secondary electron emission in the scanning electron microscope. *J. Appl. Phys.* **1983**, *54* (11), R1−R18.
(28) Covey, T. Where have all the ions gone, long time passing? Tandem quadrupole mass spectrometers with atmospheric pressure ionization sensitivity gains since the mid-1970s. A perspective. *Rapid Commun. Mass Spectrom.* **2022**, No. e9354.
(29) Mansour, A. N. Nickel monochromated Al Kα XPS spectra from the Physical Electronics Model 5400 Spectrometer. *Surf. Sci. Spectra* **1994**, *3* (3), 221−230.
(30) Biesinger, M. C.; et al. Resolving surface chemical states in XPS analysis of first row transition metals, oxides and hydroxides: Cr, Mn, Fe, Co and Ni. *Appl. Surf. Sci.* **2011**, *257* (7), 2717−2730.
(31) Kaichev, V. V.; et al. In situ XPS study of self-sustained oscillations in catalytic oxidation of propane over nickel. *Surf. Sci.* **2013**, *609*, 113−118.
(32) Blume, A. R.; et al. Structural and chemical properties of NiOx thin films: The role of oxygen vacancies in NiOOH formation in a H_2O atmosphere. *Phys. Chem. Chem. Phys.* **2023**, *25* (37), 25552−25565.
(33) O'Connor, C. R.; Boscoboinik, J. A.; Karatok, M.; van Spronsen, M. A. Carbon monoxide, CO(g), by high-resolution near-ambient-pressure X-ray photoelectron spectroscopy. *Surf. Sci. Spectra* **2020**, *27* (1), 014002.
(34) Tomellini, M. X-ray photoelectron spectra of Defective Nickel Oxide. *J. Chem. Soc., Faraday Trans. 1* **1988**, *84* (10), 3501.
(35) Gonzalez-Elipe, A. R.; Holgado, J. P.; Alvarez, R.; Munuera, G. Use of factor analysis and XPS to study defective nickel oxide. *J. Phys. Chem.* **1992**, *96* (7), 3080−3086.
(36) Mansour, A. N. Characterization of NIO by XPS. *Surf. Sci. Spectra* **1994**, *3* (3), 231−238.
(37) Colbea, C.; et al. Development of a compact laser-based heating stage for in situ spectroscopic characterizations. *Surf. Interface Anal.* **2024**, *56* (5), 283−292.
(38) Guo, M.; Dongfang, N.; Iannuzzi, M.; van Bokhoven, J. A.; Artiglia, L. Structure and Reactivity of Active Oxygen Species on Silver Surfaces for Ethylene Epoxidation. *ACS Catal.* **2024**, *14*, 10234−10244.
(39) Vesselli, E.; et al. Hydrogen-assisted transformation of CO2 on nickel: The role of formate and carbon monoxide. *J. Phys. Chem. Lett.* **2010**, *1* (1), 402−406.
(40) Zhang, X.; et al. A stable low-temperature H_2-production catalyst by crowding Pt on α-MoC. *Nature* **2021**, *589* (7842), 396−401.
(41) Akhter, S.; White, J. M. Stabilization of C_2D_X fragments by CO on Ni(100). *Surf. Sci.* **1987**, *180* (1), 19−46.
(42) Verhoeven, J. A. T.; Van Doveren, H. An XPS investigation of the interaction of CH_4, C_2H_2, C_2H_4 and C_2H_6 with a barium surface. *Surf. Sci.* **1982**, *123* (2−3), 369−383.
(43) Rameshan, R.; et al. Near-ambient-pressure X-ray photoelectron spectroscopy study of methane-induced carbon deposition on clean and copper-modified polycrystalline nickel materials. *J. Phys. Chem. C* **2015**, *119* (48), 26948−26958.
(44) Yeh, J. J.; Lindau, I. Atomic subshell photoionization cross sections and asymmetry parameters: $1 \leqslant Z \leqslant 103$. *At. Data Nucl. Data Tables* **1985**, *32*, 1−1555.
(45) Kaichev, V. V.; et al. Evolution of self-sustained kinetic oscillations in the catalytic oxidation of propane over a nickel foil. *J. Catal.* **2016**, *334*, 23−33.
(46) Bayer, B. C.; et al. In situ observations of phase transitions in metastable nickel (carbide)/carbon nanocomposites. *J. Phys. Chem. C* **2016**, *120* (39), 22571−22584.
(47) Bai, Y.; Kirvassilis, D.; Xu, L.; Mavrikakis, M. Atomic and molecular adsorption on Ni(111). *Surf. Sci.* **2019**, *679*, 240−253.
(48) Andersson, K.; et al. Bridging the pressure gap in water and hydroxyl chemistry on metal surfaces: The Cu (110) case. *J. Phys. Chem. C* **2007**, *111* (39), 14493−14499.
(49) Kidambi, P. R.; et al. Observing graphene grow: Catalyst−graphene interactions during scalable graphene growth on polycrystalline copper. *Nano Lett.* **2013**, *13* (10), 4769−4778.
(50) Alstrup, I. A new model explaining carbon filament growth on nickel, iron, and Ni-Cu alloy catalysts. *J. Catal.* **1988**, *109*, 241−251.
(51) Lahiri, J.; et al. Graphene growth on Ni(111) by transformation of a surface carbide. *Nano Lett.* **2011**, *11* (2), 518−522.
(52) Koel, B. E.; et al. The adsorption and decomposition of ethylene on Ni(100). *Chem. Phys. Lett.* **1982**, *88* (2), 236−242.
(53) Hammer, L. On the kinetics of hydrocarbon decomposition on the Ni(111) surface—a time-resolved HREELS study. *Vacuum* **1990**, *41* (1−3), 121−123.
(54) Sacco, A., Jr.; et al. Carbon deposition and filament growth on Fe, Co, and Ni foils using CH_4-H_2-H_2O-CO-CO_2 gas mixtures. *J. Catal.* **1989**, *119* (2), 322−341.
(55) Morozova, O. S.; et al. Peculiarities of nickel oxide structure transformation upon CO hydrogenation.I. initial period of Catalyst Activation. *J. Catal.* **1993**, *144* (1), 50−59.
(56) Morozova, O. S.; Kryukova, G. N.; Shashkin, D. P. Peculiarities of nickel oxide structure transformation upon co hydrogenation. *J. Catal.* **1996**, *158* (1), 13−22.
(57) NIST Office of Data and Informatics. Carbon Monoxide, National Institute of Standards and Technology, webbook.nist.gov/cgi/cbook.cgi?ID=C630080&Mask=200#Mass-Spec. (Accessed 25 September 2024).
(58) NIST Office of Data and Informatics. *Carbon Dioxide*; National Institute of Standards and Technology, webbook.nist.gov/cgi/cbook.cgi?ID=C124389&Units=SI&Mask=200#Mass-Spec. (Accessed 25 September 2024).
(59) NIST Office of Data and Informatics. Ethylene, National Institute of Standards and Technology, webbook.nist.gov/cgi/cbook.cgi?ID=C74851&Units=SI&Mask=200#Mass-Spec. (Accessed 25 September 2024).
(60) Orlando, F.; et al. The environmental photochemistry of oxide surfaces and the nature of frozen salt solutions: A new in situ XPS approach. *Top. Catal.* **2016**, *59*, 591−604.
(61) Roy, K.; Artiglia, L.; Van Bokhoven, J. A. Ambient pressure photoelectron spectroscopy: Opportunities in catalysis from solids to liquids and introducing time resolution. *ChemCatchem* **2018**, *10* (4), 666−682.

https://doi.org/10.1021/acscatal.4c04437
ACS Catal. 2024, 14, 17850−17861